

Segmented Composite Design of Robust Single-Qubit Quantum Gates

Ido Kaplan ^{*},¹ Muhammad Erew ^{*},² Yonatan Piasetzky,² Moshe Goldstein,² Yaron Oz,² and Haim Suchowski²

¹*School of Electrical Engineering, the Iby and Aladar Fleischman
Faculty of Engineering, Tel-Aviv University, Tel-Aviv 6997801, Israel.*

²*Raymond and Beverly Sackler School of Physics and Astronomy, Tel-Aviv University, Tel-Aviv 6997801, Israel.*

(Dated: October 24, 2023)

Over the past few decades, quantum information processing research has focused heavily on error mitigation schemes and error-correcting codes. However, while many proposed schemes have been successful in mitigating errors, most of them are perturbative and assume deterministic systematic errors, leaving studies of the problem considering the full noise and errors distribution scarce. In this work, we introduce an error mitigation scheme for robust single-qubit unitary gates based on composite segmented design that accounts for the full distribution of the physical noise and errors in the system. We provide two optimization approaches to construct these robust segmented gates: perturbative and non-perturbative, which address all orders of errors. We demonstrate the effectiveness of our scheme in the photonics realm for the dual-rail directional couplers realization. Specifically, we show that the 3-segmented composite design for the fundamental single-qubits unitary operations reduces the error by an order of magnitude for a realistic distribution of errors. Moreover, we demonstrate that the two approaches are compatible for small errors, and significantly reduce the overhead of modern error correction codes. Our methods are rather general and can be applied to other realizations of quantum information processing units.

I. INTRODUCTION

The potential exponential speedup for solving hard computational problems and the possible real-time capability to decrypt classical encryption protocols are the driving forces behind the tremendous research effort invested in quantum information processing (QIP) and quantum computing [1–4]. Over the last several decades, major theoretical breakthroughs have been achieved, developing quantum algorithms with applications in a variety of problems and fields, including algorithms for combinatorial optimization, quantum machine learning, decryption protocols, and variational quantum algorithms to find the ground state energy of Hamiltonian systems such as molecules [5, 6]. Yet, the realization of a quantum information processor is still far away. The major obstacles lie in the inherent systematic errors and stochastic noise of the physical building blocks, which influence state preparation through the measurement process or the unitary operations (gates), the basic ingredients of any quantum algorithm.

The problem of errors and noise is usually dealt with by error mitigation schemes or error-correcting codes. In the former, one attempts to reduce the error using various algorithmic schemes, typically with a small overhead [7–19]. In the latter, one constructs logical qubits or quantum gates using many physical qubits, with redundancy and significant overhead that ensures that the logical qubit significantly outperforms the physical qubit [20]. Most relevant error-correcting codes are stabilizer codes [7], a prime example being the surface code, having relative tolerance to local errors [8, 9]. Yet, the capability of fault-tolerant quantum computation of the surface

code is conditioned: the probability of errors has to be under certain thresholds for each operation, e.g., single-qubit gates or double-qubit gates [7–19]. High-fidelity physical gates are thus extremely important for realizing a useful error-correcting code. An important step towards fault-tolerant quantum computation is to increase the fidelity of single quantum operations, the single unitary gates, which are fundamental building blocks of QIP. This is challenging in the experimental realizations of QIP, where the slightest fabrication defects or an inaccurate coupling strength can lead to errors that include deviations from target driving amplitudes and frequencies.

In recent years, several studies have proposed schemes to enhance the robustness of state-to-state processes [21–31] and to devise robust unitary gates in various realizations of quantum information processing (QIP) [32–39]. One of the leading concepts in robust designs is based on the principles of composite pulse sequences used in atomic physics and nuclear magnetic resonance. These sequences use a combination of constant pulses to minimize errors during the evolution of quantum systems [21–24, 40]. These techniques utilize a perturbative expansion of the gate’s operation in small deterministic systematic errors and mitigate the errors order by order. Typically, these schemes deal with varying one parameter of the Hamiltonian. Another variant of this framework for error mitigation is control theory and optimal control. In this approach, an optimal path in the control parameter space is specified to construct a required quantum state from a given initial state or an approximation in the norm sense to a required quantum gate [41–45]. However, the control parameters are usually treated as deterministic, or have only one stochastic parameter.

Recently, an expansion of the technique of composite pulses has been proposed to include the full param-

* These authors contributed equally to this work.

ter space. Specifically, in integrated photonic-based QIP, which utilizes photons as low-noise carriers of quantum information in the dual-rail representation, fabrication may cause geometrical errors that primarily influence the Hamiltonian's diagonal part. A recent proposed robust solution for state-to-state directional couplers based on composite segmented couplers of different widths [31] was experimentally demonstrated [39]. The design approach showed that modifications to the fabrication protocols are not required.

However, all these proposed composite schemes deal with deterministic errors and noise, whereas, in reality, noise is random by its nature, with randomness inherited from the quantum world, thermodynamic fluctuations, and from errors in manufacturing, preparation, and measurement. These issues become even more acute when dealing with a realization of robust unitary gate operations needed to allow full operation and control of quantum information processors, with a high-enough accuracy to comply with a specific target design for each physical realization. For photonic based realization, for example, this target accuracy is the fourth decimal point [46–49], a target that places stringent fabrication tolerances on process parameters such as etching depth, waveguide widths, etc., which are challenging to meet in practice. While the current known perturbative schemes have succeeded to construct robust gates for the realization of robust unitary gate operations, treatment of the statistical nature of noise and errors is still lacking.

Here we present a scheme for robust unitary operations for realistic quantum platforms. In contrast with previous demonstrations of robust unitary gate designs, we provide protocols that consider the statistical nature of noise and errors in physical systems, and *all* orders of jointly distributed random errors. In devising our robust unitary gates, we follow two design paths. The first one is based on a perturbative approach, where we reduce the fully correlated error order by order in perturbation theory. The second is a non-perturbative method, where we search for the local maxima of the fidelity cost function so that we optimize while accounting for all orders of errors or their variances simultaneously. In order to show the great applicability of our framework, we apply both methods to the photonic dual-rail realization, providing robust high-fidelity unitary solutions to different single-qubit gates, including the fundamental X , $X^{\frac{1}{2}}$, $X^{\frac{1}{3}}$ and Hadamard gates. We demonstrate that the unitary segmented solutions are effective and compatible in practical scenarios of directional-couplers realizations, and are far more robust to systematic errors as compared to uniform couplers. Furthermore, we present the advantage of utilizing optimized segmented couplers in reducing the the logical error of the logical state of surface codes by order of magnitude. Moreover, we show that incorporating these gates in a quantum circuit, such as the QFT algorithm circuit, increases the robustness of entire circuits. This presents a significant advancement over previous works that only focus on correcting errors

in individual gates. Our error mitigation techniques have practical applications that can improve the performance of complex quantum algorithms. While we take the integrated photonics path-encoded qubits realization as an example to illustrate the strengths of the scheme on-chip building blocks for quantum applications, the method is rather general and can be applied to any other realization of a QIP device.

Our paper is organized as follows: In Section II, we present the single qubit gates and our methods for designing robust ones for a general statistical error model, and illustrate them for an example error model. In Section III, we describe how single qubit gates are physically realized in integrated photonics, describe the error model in the integrated photonics realization, and, using our methods, find and design several robust gates according to a statistical model of fabrication errors in the manufacturing process. We further show how the logical error in a surface code, as a consequence, would behave given our solutions and an error model. In Section IV, we summarize and discuss our results. In the appendixes, we provide details of the calculations and further information on various solutions.

II. METHOD AND ILLUSTRATION ON A REDUCED ERROR MODEL

A. Single Qubit Quantum Gates and Fidelity

The time evolution of a general qubit system $\{|0\rangle, |1\rangle\}$ is governed by the Schrödinger equation:

$$i\partial_t \begin{pmatrix} c_1(t) \\ c_2(t) \end{pmatrix} = \begin{pmatrix} -\Delta(t) & \Omega^*(t) \\ \Omega(t) & \Delta(t) \end{pmatrix} \begin{pmatrix} c_1(t) \\ c_2(t) \end{pmatrix}, \quad (1)$$

where $c_1(t)$ and $c_2(t)$ are the probability amplitudes at time t of the states $|0\rangle$ and $|1\rangle$ respectively, $\Omega(t)$ is the (complex) Rabi frequency, $\Delta(t)$ is the (real) detuning, and we set $\hbar = 1$. The unitary propagator of such a system is:

$$U(t, 0) = \mathcal{T} \left[\exp \left[-i \int_0^t \begin{pmatrix} -\Delta(t') & \Omega^*(t') \\ \Omega(t') & \Delta(t') \end{pmatrix} dt' \right] \right]. \quad (2)$$

When Ω and Δ are independent of time, the propagator simplifies to:

$$U(t, 0) = \exp \left[-it \begin{pmatrix} -\Delta & \Omega^* \\ \Omega & \Delta \end{pmatrix} \right]. \quad (3)$$

Using physical systems that follow such $SU(2)$ dynamics, one can implement various single qubit gates. However, when one considers noise in the physical system, the implemented gate deviates from the desired one. In order to quantify how far the noisy gate is from the desired one, we will consider the metric provided by the fidelity F of the gate $U(\epsilon)$, which is defined as

$$F(U_{\text{ideal}}, U(\epsilon)) = \frac{1}{2} |\text{Tr}(U_{\text{ideal}}^\dagger U(\epsilon))|, \quad (4)$$

where U_{ideal} is the desired ideal unitary gate given by Eq. (3), and $U(\epsilon)$ is its actual physical realization, which depends on a set of jointly distributed random errors, $\epsilon = \{\epsilon^a\}_{a=1}^m$. This fidelity takes values in the interval $[0, 1]$, where 1 corresponds to the case of no errors, and 0 corresponds to the case of maximal deviation from the desired unitary gate operation.

The goal in this work is to increase the expectation value of the fidelity:

$$\bar{F} = \mathbb{E}_\epsilon[F(U_{\text{ideal}}, U(\epsilon))] . \quad (5)$$

This will be done both for the general case as well as for a specific statistical error model of integrated photonic realm. The relevant statistical error model should be taken depending on the specific physical realization of the gates, where one considers the quantum errors, thermodynamic errors, and the errors of manufacturing, preparation, and measurement. Maximizing the mean fidelity over a wide error range is crucial for fault-tolerant computation, as mentioned in the introduction, since a certain threshold for the resulting physical error probability has to be achieved.

B. Constructing Robust Composite Gates

The method that we employ to design robust gates is to compose pulses or segments. The reasoning behind this approach is the natural assumption that the relevant errors are highly correlated, and this correlation can be applied to cancel errors with appropriately tuned designs. Consider an ideal unitary gate U_{ideal} , as well as its actual noisy segmented realization $U^{(N)} = \prod_{k=1}^N U_k(\epsilon_k)$, where ϵ_k is the random error vector of the k^{th} segment, which includes m errors: $\epsilon_k = \{\epsilon_k^a\}_{a=1}^m$. All the errors are jointly distributed random variables. Each segment U_k without errors is as in Eq. (3). The goal is to increase the expectation value of the fidelity in Eq. (5).

In our analysis, we employ two methods. The first one is perturbative in the error random variables, where we consider them to be fully correlated and design the segmented gate such that we cancel the errors order by order in perturbation theory. More specifically, we construct analytical solutions of 3-segmented designs that cancel the first order error term. Clearly, cancellation of higher order error terms requires a larger number of segments.

The second method is non-perturbative, where we consider Eq. (5) as a cost function to be maximized. While these two methods are compatible for small errors or small variances of errors, as will be seen, the non-perturbative approach also offer a path for addressing large values of the random error variances, where the optimization take into account all orders in the errors simultaneously.

C. Example: A detuning Error Model

In order to illustrate our methods in a relatively simple case, we consider first a physical system which allows only real Ω 's, and we assume a single error random variable $\epsilon_k = \epsilon$, $k = 1, \dots, N$, which is a systematic error in Δ , and neglect the error in Ω . We further assume that the errors of the different segments are fully correlated. This assumption describes well the errors in several quantum and classical systems that follow such SU(2) dynamics, such as gates of trapped ions [25, 26], sum-frequency generation [50], atomic systems [27–29], etc.

The N -segmented gate reads:

$$U^{(N)} = \prod_{k=1}^N U(\Omega_k, \Delta_k, t_k, \epsilon) , \quad (6)$$

where

$$U(\Omega, \Delta, t, \epsilon) = e^{-it(\Omega X - \Delta Z - \epsilon Z)} , \quad (7)$$

and t_k, Ω_k, Δ_k are the length of the k^{th} -segment, its coupling, and its detuning, respectively. The N -segmented gate fidelity (4) is $F(U^{(N)}(0), U^{(N)}(\epsilon))$.

1. Perturbative Method

In the perturbative approach, we consider the error in the quantum gate

$$E(\epsilon) = U(\epsilon) - U(0) = \sum_{k>0} E_k \epsilon^k . \quad (8)$$

The task is to design an N -segmented gate U such that $E = O(\epsilon^n)$ for a given n . In many practical realizations, it is sufficient to take $n = 2$. Note that since $E(\epsilon)$ is a function of a random variable instance, removing the linear order term is not simply removing the expectation value of ϵ .

Let us take for example $U = X$, and construct the gate up to an overall phase, that is, iX . We need to find N and $\{\Omega_k\}_{k=1}^N, \{\Delta_k\}_{k=1}^N, \{t_k\}_{k=1}^N$ such that $U^{(N)}(0) = iX$, $\left. \frac{\partial E^{(N)}(\epsilon)}{\partial \epsilon} \right|_{\epsilon=0} = 0$, $\left. \frac{\partial^2 E^{(N)}(\epsilon)}{\partial \epsilon^2} \right|_{\epsilon=0} = 0$, etc. Using the unitarity of each propagator one can simplify the equations and reduce their complexity. In Appendix A we present analytical robust solutions of the equations for the gates of the form $(iX)^{\frac{1}{n}}$, where n is a positive integer, employing three segments, and two solutions of the iX gate using four segments with the same coupling constant. We also compare in Appendix A our solutions' fidelity to that of a single segment for $n = 1, 2, 3$.

2. Non-Perturbative Method

In the non-perturbative approach, we search for a maximum of a cost function (minimum of a loss function) by

optimization. In order to simplify the optimization process, we split the loss function into two subfunctions, the *invalid range loss subfunction* and the *robust fidelity loss subfunction*. The former ensures that the parameters we obtain are within their allowed range (for instance, the length of the waveguides cannot be negative) by strongly penalizing deviations from it. The robust fidelity loss subfunction calculates the fidelity for a range of N error values between -3σ to 3σ , σ being the standard deviation, and weighs these fidelities according to the assumed error distribution (for instance, a normal distribution). An overall minus sign is added in order for the algorithm to minimize this value and thus maximize the overall fidelity. For example, the loss function used for errors that have a normal distribution is:

$$\begin{aligned} \text{Loss} = & 1 - \sum_{x=-3\sigma}^{3\sigma} \frac{e^{-\frac{x^2}{2\sigma^2}}}{\text{Dist}_{\text{sum}}} \cdot F(U_{\text{ideal}}, U_{\text{optimization}})(x) \\ & + \mu \cdot \sum_{i=0}^{N-1} \sum_{j=0}^{m-1} \max(0, p_{j,i} - p_j^{\text{Max}}) + \max(0, p_j^{\text{Min}} - p_{j,i}), \end{aligned} \quad (9)$$

The former sum in the loss function is discrete: between each pair of subsequent x values there's an interval of $\frac{1}{n}$, where $n+1$ is the number of samples used to estimate the integral. The value $\text{Dist}_{\text{sum}} = \sum_{x=-3\sigma}^{x=3\sigma} e^{-\frac{x^2}{2\sigma^2}}$ is used to normalize the distribution function, which guarantees that the robust fidelity loss subfunction's minimal value is 0. μ defines the weight ratio between the loss subfunctions. There are N segments used, with m parameters per segment (for instance, in this model, $m=3$ because there are three parameters: Ω, Δ, t). p is the selected parameter values. p_j^{Min} and p_j^{Max} are chosen by physical limitations (for instance, $t^{\text{Min}} = 0$, since the length of the waveguides cannot be negative) and μ is set to be in the range of $[5, 100]$.

By minimizing these two subfunctions, we obtain physically feasible parameters which minimize the fidelity loss for errors between -3σ to 3σ weighted by the given error distribution. Furthermore, the optimizer we used is the Adam optimizer [51] (Adaptive Moment Estimation optimizer), which is an optimizer that computes individual adaptive learning rates for different parameters from estimates of first and second moments of the gradients. The initial learning rate we used is 10^{-3} .

Examples of non-perturbative solutions for the detuning error model and their simulations can be seen in Appendix B. We show in Fig. 1(a-b) one solution on the Bloch sphere compared to the uniform gate, as well as how errors affect the result of the gate for two different initial states for each case (uniform and composite).

Further details regarding the optimization process are described in Appendix C.

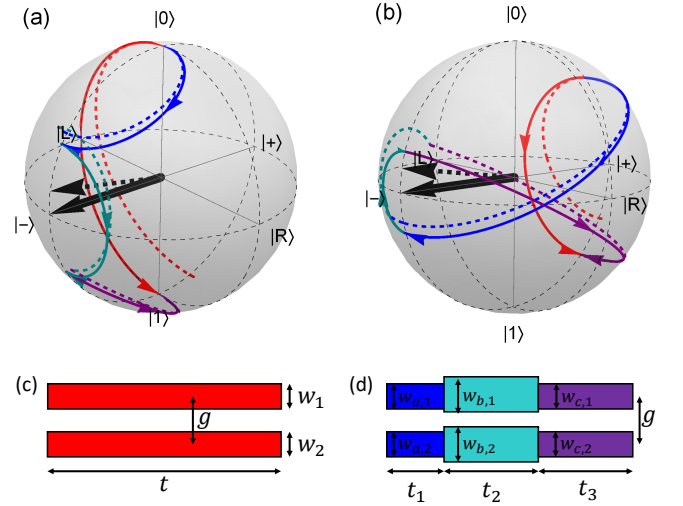


FIG. 1. Naïve vs. composite gate. (a-b) Bloch sphere representation of a robust composite $-iX$ Gate. The plot provides a schematic description of two different states on Bloch sphere and the trajectories they follow under the uniform $-iX$ gate (in continuous red), and under the segmented gate presented in Table V (in continuous blue, turquoise, and purple). In dashed lines, we show the trajectories the states follow when an error $\epsilon = 0.17\Omega$ occurs simultaneously in all detunings. In black, we depict the torque vector of the uniform gate around which the states rotate under the $-iX$ operation. One can see the robustness of the segmented gate against such errors compared to the uniform regular gate. We show this for two different initial states, $|0\rangle$ and $\cos(\frac{\pi}{8})|0\rangle + \sin(\frac{\pi}{8})|1\rangle$, to emphasize that the whole gate is robust, not only the complete population transfer between $|0\rangle$ and $|1\rangle$. In other words, the $-iX$ gate is robust for any initial state; i.e. not only the magnitude of the element U_{12} of the representative matrix of the operation is robust (against errors in the physical system) but also its phase, as well as the phase of the element U_{11} . (c-d) Dual rail photonic realization of unitary gates. Schematic 2D top view illustrations of standard and composite gates respectively, based on the directional couplers realization of gates in integrated photonics. We denote the waveguides widths w_1, w_2 , the length t and the gap g .

III. ROBUST SEGMENTED GATES IN INTEGRATED PHOTONICS

As there are several realizations of quantum gates and each one has an appropriate statistical model of errors, we choose, the following, to apply our methods to the photonic realm [47–49]. This realm, which utilizes photons as excellent low-noise carriers of quantum information, requires that unitary gate comply with a target design to a fourth decimal point accuracy[46].

A. Directional Couplers as Gates and their Error Model

According to the coupled-mode theory, the propagation of the pair of electrical fields $E_{1,2}$ in a directional coupler of a fixed cross-section is described exactly by Eqs. (1) and (3), where the actual matrix elements that describe the dynamics along the two waveguides are the mode propagation constants' mismatch $\Delta\beta$ and the interaction coupling κ between the two waveguides [50]. The coupling coefficient κ between the waveguides is equivalent to the off-diagonal term Ω . The mode mismatch between the mode index $\Delta\beta = \beta_1 - \beta_2$ is equivalent to the diagonal term Δ , and the propagation length z , is equivalent to the evolution time t . The coupling κ is largely determined by the distance between the cores.

In our analysis of the functional dependence of the coupling, the detuning, and the relevant error model, we solve for the realization of single-mode silicon-on-insulator rib waveguides. The parameters Ω and Δ in Eqs. (1) and (3) are in fact functions of the following physical parameters, some of which are depicted in Fig. 1(c),(d):

1. h_1, h_2 — Etching depths,
2. w_1, w_2 — The widths of the waveguides,
3. H_1, H_2 — The heights of the waveguides,
4. g — The gap between the waveguides,
5. T — The temperature,
6. λ — The wavelength.

waveguide devices can support low-loss bends, down to some finite radius, mostly determined by the refraction index contrast between the core and the cladding of the waveguide. Below this radius, significant losses occur due to scattering from wall roughness and radiation loss from the curvature of the waveguide [52]. Typical Silicon on Insulator (SOI) devices usually allow a bend radius to be no smaller than roughly 10 microns. This results in difficulty in applying significant gap changes abruptly (i.e., within a distance that is considerably less than the length of a segment). Thus, in our designs we aimed for a fixed gap for all the different segments. For a fixed gap, etching depth, temperature, wavelength, and waveguide heights:

$$\Omega = \kappa(w_1, w_2), \quad (10a)$$

$$\Delta = \Delta\beta(w_1, w_2). \quad (10b)$$

In order to estimate these functions, i.e., the mode propagation mismatch and coupling coefficients as functions of the geometric components for a desired range of values, we used the coupled mode theory approximation, Lumerical simulations, and known fitting methods. For details, see Appendix D.

We assume that for the desired set of widths of the waveguides, they all have the same error, i.e. they are fully correlated, and this error is distributed normally:

$$\delta w \sim \mathcal{N}(0, \sigma^2), \quad (11)$$

independently of the value of the desired set of widths. We describe our perturbative method in Section III B 1, and the non-perturbative numerical search in Section III B 2.

B. Methodology

Using the interpolation functions for the dependence of κ and $\Delta\beta$ on the parameters, and assuming all segments have the same error in widths, the error model can be dealt with perturbatively in a simple way. We define the k th segment of the N -segmented gate by

$$U_k = e^{-i\frac{z_k}{2}(\kappa(w_{1k}+\delta w, w_{2k}+\delta w)X - \Delta\beta(w_{1k}+\delta w, w_{2k}+\delta w)Z)}, \quad (12)$$

where z_k, w_{1k}, w_{2k} are its length and widths respectively. The N -composite gate reads:

$$U^{(N)}(\delta w) = U_c \left(\prod_{k=1}^N U_k \right) U_c, \quad (13)$$

where the matrix U_c represents the non-zero coupling effect that occurs when the two waveguides are brought closer and taken further away. We model this effect as another segment at the beginning and the end of the composite segment design, with zero detuning, given by

$$U_c = \cos(\theta_c)I - i \sin(\theta_c)X. \quad (14)$$

The parameter $\theta_c = 0.232$ was determined numerically following [53], and verified experimentally by fabricating various zero detuning directional couplers with an identical cross-section, measuring the coupling ratio, extrapolating the coupling ratio to zero coupling length, and finally estimating the amount of coupling that occurs only from initiating and terminating the interaction.

1. Perturbative Method

We seek solutions that make the derivatives vanish:

$$\left. \frac{\partial^j U^{(N)}(\delta w)}{\partial \delta w^j} \right|_{\delta w=0} = 0, \quad (15)$$

for $j = 1, 2, 3, \dots$. When we find a solution, we will provide a plot of its fidelity based on this simplified model, and a plot of its fidelity based on the model described in Section III A. One can see from Fig. 3 that it is sufficient for our purposes to work with the former one. This is due to the assumption that $\sigma < 20$ nm, which is much smaller than w_1, w_2 .

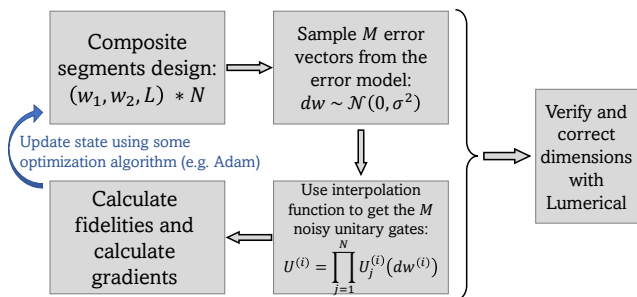


FIG. 2. **The non-perturbative optimization method.** In this method, we initialize our composite design with some randomly chosen geometric parameters. We then sample geometries from our error model and calculate the resulting fidelities. Using these results, we perform multiple optimization iterations until convergence to a robust design. Lastly, we analyze the resulting design back in Lumerical and fine-tune the lengths.

2. Non-Perturbative Method

For the numeric approach, we set a correlated error distribution in the waveguide widths, multiply the matrices M_i in stage 4 of the robust fidelity loss calculation described in Appendix C by U_c on both sides to simulate the coupling effect before and after the waveguides enter the directional coupler, and use the interpolation functions in order to translate between the geometric parameters and κ and $\Delta\beta$. We then optimize the geometric parameters of our segmented design, by using a stochastic gradient-based optimization method. Lastly, we analyze and verify the resulting segments in Lumerical. We also correct small discrepancies in the segment lengths that may arise between the coupled mode theory-based coupling approximation (Appendix D) and the more accurate two-waveguides simulations with Lumerical. The method for fixing this discrepancy is also explained in Appendix D. The numerical non-perturbative method is illustrated in Fig. 2.

C. Solutions

In this section, we present selected composite based designs for robust unitary gates in the integrated photonic realm. The designs, generated both for perturbative and non-perturbative approaches, are compared with the uniform coupler fidelity, which is calculated up to a global phase. The uniform coupler parameters and segmented coupler parameters are fully presented in Appendix E in tables VI and VII.

1. Random error simulations

In Figs. 3 and 4 we compare the uniform and segmented gates robustness by using width errors sampled randomly from a normal error distribution. In both simulations, 10^5 values were sampled for improved accuracy.

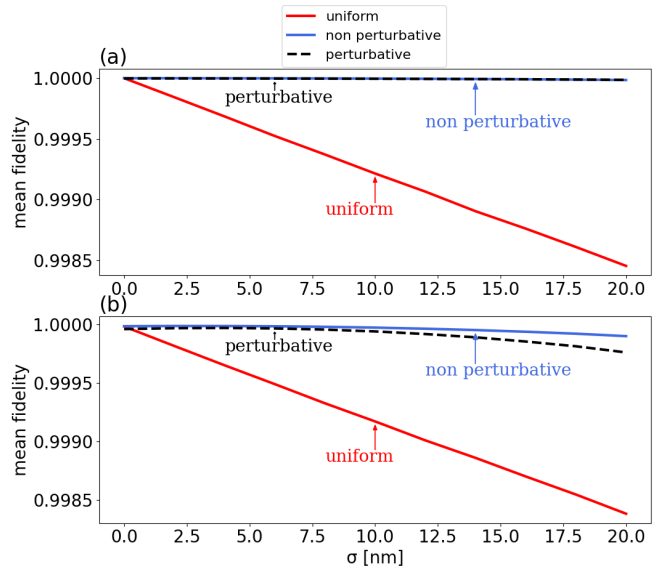


FIG. 3. The mean fidelity of the perturbative and non-perturbative composite gates compared to uniform gates, with full error correlation in the width, as a function of the error standard deviation σ . In (a) the ideal gate is X and in (b) the ideal gate is the Hadamard gate.

In Fig. 3 we compare the mean fidelity of the segmented and uniform gates, assuming fully correlated errors in all widths for all segments. As can be seen from the figure, for both the X gate and the Hadamard gate, there is a clear advantage for the segmented design, which becomes more pronounced as the standard deviation increases.

In Fig. 4 we compare the standard deviation of the fidelity of the segmented and uniform gates, assuming again fully correlated errors in all widths for all segments. We see that for every σ value in the given range, the standard deviation of the fidelity of the segmented design is lower than that of the uniform one. Furthermore, we can see that for the X gate simulation (Fig. 4 (a)), as the value of σ increases, the difference in fidelity standard deviation between the segmented and uniform design rises linearly. This means that compared to the uniform design, the segmented design is far less likely to suffer from random fidelity values lower than the mean fidelity, even when the average width error in the waveguides is greater.

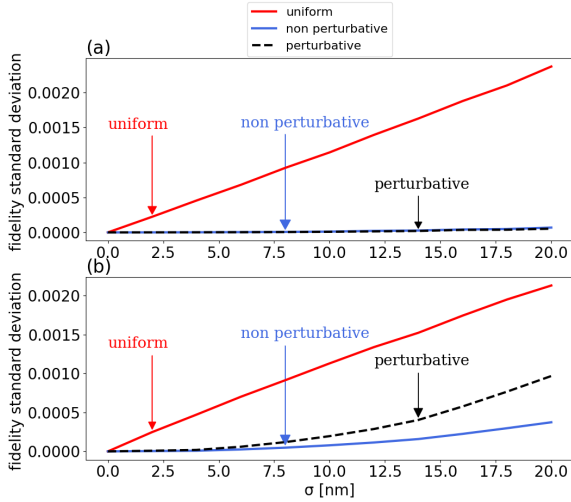


FIG. 4. The standard deviation of the fidelity for uniform couplers compared to segmented couplers, with full error correlation in the width, as a function of the error standard deviation σ . In (a) the ideal gate is X and in (b) the ideal gate is the Hadamard gate.

2. Deterministic error simulations

In Fig. 5 we compare the uniform and segmented gates robustness for fixed deterministic errors. In the simulations, the fidelity of both uniform and segmented couplers was calculated for multiple error values between -20 nm and 20 nm, that is between -3 and 3 standard deviations. As shown for the random error simulations, the fidelity of the segmented design is far more robust in comparison to the uniform one. Furthermore, for both the perturbative and non-perturbative approaches, the difference between the fidelity of the uniform and segmented couplers increases in a parabolic fashion as σ increases.

As seen clearly in the figures in this section, the segmented designs are more robust than the uniform ones, having higher fidelity mean and lower fidelity variance.

D. Logical Error

The error reduction shown in Fig. 3 and 5 demonstrates the mitigation of correlated physical errors, and is evidently important during the Noisy Intermediate-Scale Quantum quantum computation (NISQ) era [54], in which a significant error reduction allows an order of magnitude increase in the number of operations one could perform before the circuit becomes too noisy. Moreover, and even much more crucial, error mitigation is also of much relevance to fault-tolerant quantum computers, where a quantum error-correcting code is implemented. Consider for instance the surface code (for a review see [55]). The logical error P_L is related to the physical error p by the empirical formula:

$$P_L \sim (p/p_{\text{th}})^{d_e}, \quad (16)$$

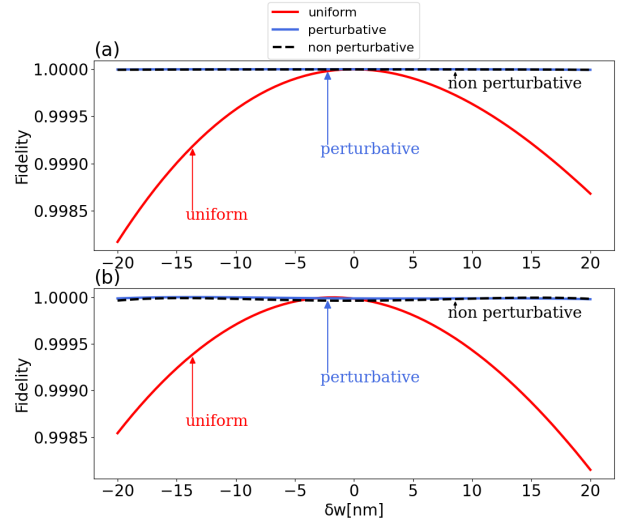


FIG. 5. The fidelity of the perturbative and non-perturbative composite gates compared to uniform gates for a fixed error value in the waveguide widths, δw . In (a) the ideal gate is X and in (b) the ideal gate is the Hadamard gate.

where p_{th} is the surface code threshold and is estimated as 0.57%, d is the size of the surface array, and $d_e = (d + 1)/2$ is the code distance. Using equation 16, we can estimate how close are the uniform and segmented couplers' error rate to the empirical surface code threshold for single-qubit gates.

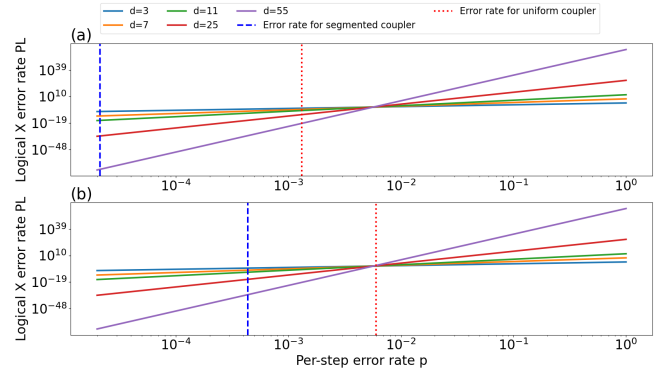


FIG. 6. The logical error rate P_L as a function of the physical error rate p , tested on X gate using a surface code. In (a) the width error is set to be 3 standard deviations while in (b) the width error is set to be $\sim 15\%$ of the nominal width (roughly 9 standard deviations). The dashed vertical line denotes the threshold of the quantum error correcting code.

To estimate the physical error rate p , we employed a large number of single logical qubit states ψ . For each error rate estimation, we generated 10,000 uniformly random ψ states, where each ψ is defined as

$$|\psi\rangle = \frac{|\psi_r\rangle}{\sqrt{\langle\psi_r|\psi_r\rangle}}, \quad (17)$$

with $\psi_r = (a_r + ia_i)|0\rangle + (b_r + ib_i)|1\rangle$. Here, a_r , a_i , b_r ,

and b_i are sampled from a uniform distribution between 0 and 1. Subsequently, we computed the physical error rate for each ψ using the formula

$$p_\psi = |\langle U\psi, U_{\text{ideal}}\psi \rangle|. \quad (18)$$

Finally, our physical error rate p was determined as the minimum value within this range:

$$p = \min_{\psi}(p_\psi). \quad (19)$$

The results of this numerical estimate can be seen in Fig. 6, where the parameters used for this optimization are given in table VII. In Fig. 6 (a) the physical error rates for uniform and segmented couplers are smaller than the threshold, meaning the logical error in both couplers can be reduced by using the surface code error correction. However, the ratio between the logical error rates is significant and rises exponentially for increasing d values. This implies that, by using the segmented coupler, one can perform error correction efficiently and with less resources (fewer physical qubits and quantum gates). In Fig. 6 (b), while the physical error rate for the segmented coupler is still smaller than the threshold, the physical error rate for the uniform coupler is not. This means that errors generated in the uniform coupler cannot be corrected using the error-correcting surface code. Note that this result is obtained when the width error is set to be very large (above 8 standard deviations). In these simulations, we used a circuit model-based quantum error correction code and not a measurement-based quantum computation model [56]. While this can lead to inaccuracies, since the optimization model itself is applicable to other qubit implementations (where instead of segmented couplers, we can use, e.g., composite pulses), we expect these results to be qualitatively correct for photonic systems.

E. Quantum Fourier Transform (QFT) infidelity estimation

Based on our composite unitary gates, here we show the great improvement in the realization a real quantum algorithm. We choose the QFT, which is basic and critical quantum algorithm in many state-of-the-art quantum algorithms, such as Shor's algorithm.

In Figure 7 (a), we present a model which enables the estimation of the QFT circuit infidelity. We first replace all single qubit gates with directional couplers with given waveguide width error. Afterwards, we initialize the circuit with state: $QFT_{\text{inv}}|0_00_1\dots0_{n-1}\rangle$. Finally, we run the QFT algorithm with the noisy gates and measure the outcome. If the width error is 0, then the algorithm's output will be state $|0_00_1\dots0_{n-1}\rangle$. Using this notion, we calculate the circuit's infidelity in the following manner: $INF_{QFT} = \langle 0_00_1\dots0_{n-1} | QFT \cdot QFT_{\text{inv}} | 0_00_1\dots0_{n-1} \rangle$, where QFT is the QFT circuit with noisy single qubit gates.

Using this method, we numerically calculated INF_{QFT} for both the segmented and uniform directional couplers by measuring the algorithm outcomes for 1,000,000 simulations.

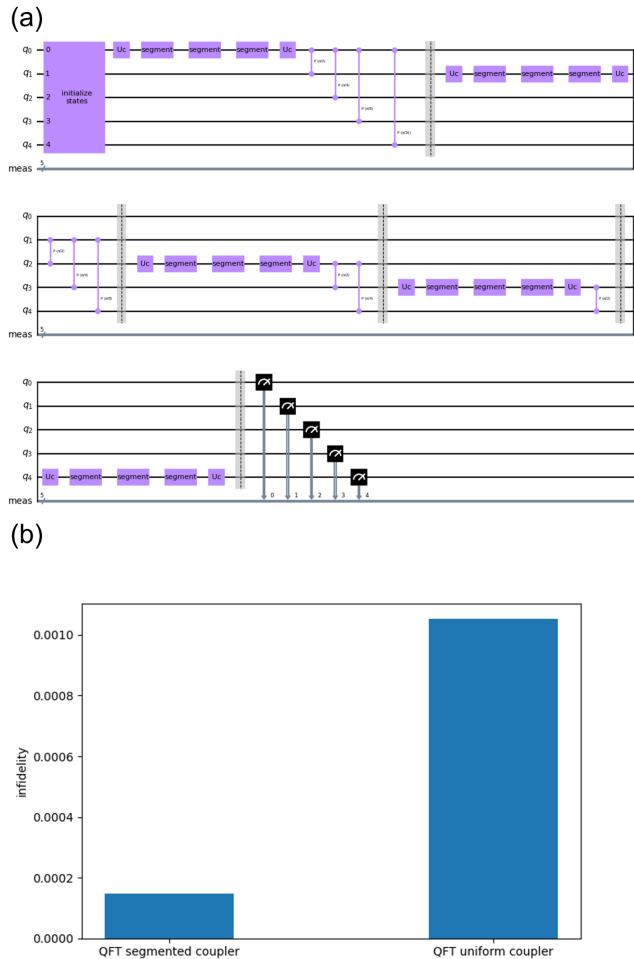


FIG. 7. Five qubit QFT algorithm. (a) A circuit-based schematic of a Five qubit QFT algorithm. Each of the gates in the algorithm is chosen to be either traditional-uniform gate or composite-based unitary gates. (b) The infidelity of the QFT circuit using segmented and uniform coupler

Employing the parameters shown in table VII, we estimated that the infidelity of the QFT circuit using the uniform couplers is 6.5 times greater than the infidelity of QFT circuit using the segmented couplers, as can be seen in Figure 7 (b).

The QFT model and our numerical verifications are available in the following Github repository: https://github.com/Ido-Kaplan/QFT_error_correction.

IV. DISCUSSION

In our research, we considered the fidelity function as a random variable which inherits its randomness by being a function that depends on fully correlated jointly distributed errors.

These errors are the systematic coherent errors due to imperfections in the construction of quantum devices. Our framework studies the mean and variance of the fidelity function with respect to the joint probability distribution function and optimizes them. The question that we address is whether segmented composite pulses allow for better fidelity properties as specified in this framework.

While our scheme combines ingredients of the composite pulse and optimal control frameworks, such as gradient ascent algorithm [57, 58] and trajectory optimization [59], it is not identical to either of them.

One could have attempted to make a mathematical mapping between the different schemes, but this would require considering the control parameters as a jointly distributed random variables with a particular auto-correlation at different discrete times. This can make the control theory framework less efficient compared to its current implementation.

The parameters generated by both approaches were compared to the uniform coupler's fidelity in two types of simulations: probabilistic simulations and deterministic simulations. In the probabilistic simulations, the mean fidelity and fidelity standard deviation is estimated for a range of different standard deviations used for the error distribution. In the deterministic simulations, the fidelity was calculated for a range of deterministic errors between -3 and 3 standard deviations (width error between -20 nm and 20 nm). In these simulations, both approaches presented parameters for segmented couplers, which were far more robust to systematic errors compared to the uniform coupler.

In the last section of the results, we show a clear connection between the reduction of the physical gate error using our optimized segmented couplers and the logical error rate PL in the quantum circuit. For a physical error of 20 nm (roughly $\sim 5\%$ of the average waveguide width), both the uniform and segmented coupler were below the threshold of the quantum error correcting code, meaning both could potentially be corrected by the error correcting codes, but the uniform coupler required many more resources (qubits and quantum gates) to do so. For a higher physical error, 60 nm (roughly $\sim 15\%$ of the average waveguide width), the segmented coupler was still below the threshold, however, the uniform coupler was not, suggesting that it could not be corrected by the quantum error correcting code such as surface code.

As mentioned in the results, we uploaded a platform which allows testing the directional coupler's fidelity robustness increase in a QFT circuit. In this platform the user can edit the geometric parameters and width error of the coupler, as well as the number of qubits used in the QFT, and observe how they affect the infidelity of the coupler.

V. CONCLUSIONS

To conclude, our composite approaches are shown to be far more robust to random systematic errors compared to the uniform coupler. We provide two approaches to construct these robust segmented gates: a perturbative approach and a non-perturbative approach, and demonstrated them in the photonic realm for the directional coupler realization of the gates. Specifically, we constructed robust designs against correlated Normally distributed width errors for the X , $X^{\frac{1}{2}}$, $X^{\frac{1}{3}}$, and H gates.

The approaches shown in this paper were demonstrated with directional couplers, but the algorithms presented are by no means limited to optic-based quantum computation — they are applicable to any quantum computing hardware, making both approaches (perturbative and non-perturbative) relevant in different quantum gate implementations as well. Furthermore, while this paper concentrates on single-qubit gates and correlated errors, we expect the methodology to apply to multi-qubit gates or gates with partial error correlation between the segments, which are worthy topics for future studies. Another important topic for further research is the evaluation of how segmented couplers can impact the success rate of success of state-of-the-art quantum error correcting codes, such as the surface code; this illustrates how the correction of systematic errors can increase the success rates of modern quantum algorithms. We believe that our segmented design for unitary gate operations and the design methods that were provided here could serve as fundamental elements and operations in many physical realizations of quantum information processing and quantum computing.

ACKNOWLEDGEMENTS

Our work has been supported by the Israel Science Foundation (ISF) and the Directorate for Defense Research and Development (DDR&D) grant No. 3427/21. M.G. has been further supported by the US-Israel Binational Science Foundation (BSF) Grant No. 2020072. The work of Y.O. is supported in part by an ISF Center of Excellence.

[1] 40 years of quantum computing. *Nature Reviews Physics*, 4(1):1–1, Jan 2022.

[2] Alán Aspuru-Guzik and Philip Walther. Photonic quantum simulators. *Nature Physics*, 8(4):285–291, Apr 2012.

- [3] G Wendin. Quantum information processing with superconducting circuits: a review. *Reports on Progress in Physics*, 80(10):106001, sep 2017.
- [4] Bjoern Lekitsch, Sebastian Weidt, Austin G. Fowler, Klaus Mølmer, Simon J. Devitt, Christof Wunderlich, and Winfried K. Hensinger. Blueprint for a microwave trapped ion quantum computer. *Science Advances*, 3(2):e1601540, 2017.
- [5] Ashley Montanaro. Quantum algorithms: an overview. *npj Quantum Information*, 2(1):15023, Jan 2016.
- [6] M. Cerezo, Andrew Arrasmith, Ryan Babbush, Simon C. Benjamin, Suguru Endo, Keisuke Fujii, Jarrod R. McClean, Kosuke Mitarai, Xiao Yuan, Lukasz Cincio, and Patrick J. Coles. Variational quantum algorithms. *Nature Reviews Physics*, 3(9):625–644, Sep 2021.
- [7] Daniel Gottesman. Stabilizer codes and quantum error correction. *arXiv: Quantum Physics*, 1997.
- [8] Sergey Bravyi and A. Yu. Kitaev. Quantum codes on a lattice with boundary, 1998.
- [9] Eric Dennis, Alexei Kitaev, Andrew J. Landahl, and John Preskill. Topological quantum memory. *Journal of Mathematical Physics*, 43(9):4452–4505, 2002.
- [10] Robert Raussendorf, Jim Harrington, and Kovid Goyal. A fault-tolerant one-way quantum computer. *Annals of Physics*, 321(9):2242–2270, 2006.
- [11] Robert Raussendorf and Jim Harrington. Fault-tolerant quantum computation with high threshold in two dimensions. *Physical review letters*, 98(19), 2007.
- [12] Robert Raussendorf, Jim Harrington, and Kovid Goyal. Topological fault-tolerance in cluster state quantum computation. *New Journal of Physics*, 9(6):199–199, 2007.
- [13] Austin G. Fowler, Ashley M. Stephens, and Peter Groszkowski. High-threshold universal quantum computation on the surface code. *Physical Review A*, 80(5), 2009.
- [14] David P. DiVincenzo. Fault-tolerant architectures for superconducting qubits. *Physica Scripta*, 2009.
- [15] Austin G. Fowler, David S. Wang, and Lloyd C. L. Hollenberg. Surface code quantum error correction incorporating accurate error propagation. *Quantum Information & Computation*, 11(1):8–18, 2011.
- [16] James R. Wootton and Daniel Loss. High threshold error correction for the surface code. *Physical review letters*, 109(16):160503–160503, 2012.
- [17] Austin G. Fowler. Analytic asymptotic performance of topological codes. *Physical Review A*, 87(4), 2013.
- [18] Sagar Vijay, Timothy H. Hsieh, and Liang Fu. Majorana fermion surface code for universal quantum computation. *Physical Review X*, 5(4):041038, 2015.
- [19] Sergey Bravyi, Matthias Englbrecht, Robert König, and Nolan Peard. Correcting coherent errors with surface codes. *npj Quantum Information*, 4(1):55, 2018.
- [20] Joschka Roffe. Quantum error correction: an introductory guide. *Contemporary Physics*, 60(3):226–245, 2019.
- [21] Malcolm H. Levitt and Ray Freeman. Nmr population inversion using a composite pulse. *Journal of Magnetic Resonance (1969)*, 33(2):473–476, 1979.
- [22] A.J Shaka and Alexander Pines. Symmetric phase-alternating composite pulses. *Journal of Magnetic Resonance (1969)*, 71(3):495–503, 1987.
- [23] Malcolm H. Levitt. Composite pulses. *Progress in Nuclear Magnetic Resonance Spectroscopy*, 18(2):61–122, 1986.
- [24] Nuala Timoney, V. Elman, Steffen J. Glaser, C. Weiss, M. Johanning, W. Neuhauser, and Chr. Wunderlich. Error-resistant single-qubit gates with trapped ions. *Physical Review A*, 77(5), 2008.
- [25] R. Ozeri, W. M. Itano, R. B. Blakestad, J. Britton, J. Chiaverini, J. D. Jost, C. Langer, D. Leibfried, R. Reichle, S. Seidelin, J. H. Wesenberg, and D. J. Wineland. Errors in trapped-ion quantum gates due to spontaneous photon scattering. *Phys. Rev. A*, 75:042329, Apr 2007.
- [26] A. E. Webb, S. C. Webster, S. Collingbourne, D. Braud, A. M. Lawrence, S. Weidt, F. Mintert, and W. K. Hensinger. Resilient entangling gates for trapped ions. *Phys. Rev. Lett.*, 121:180501, Nov 2018.
- [27] J. E. Lang, T. Madhavan, J.-P. Tetienne, D. A. Broadway, L. T. Hall, T. Teraji, T. S. Monteiro, A. Stacey, and L. C. L. Hollenberg. Nonvanishing effect of detuning errors in dynamical-decoupling-based quantum sensing experiments. *Phys. Rev. A*, 99:012110, Jan 2019.
- [28] Kevin Cox, Matthew Norcia, Joshua Weiner, Justin Bohnet, and James Thompson. Reducing collective quantum state rotation errors with reversible dephasing. *Applied Physics Letters*, 105, 07 2014.
- [29] J. Randall, A. M. Lawrence, S. C. Webster, S. Weidt, N. V. Vitanov, and W. K. Hensinger. Generation of high-fidelity quantum control methods for multilevel systems. *Phys. Rev. A*, 98:043414, Oct 2018.
- [30] Yonathan Erlich, Andon A. Rangelov, Germano Montemezzani, and Haim Suchowski. Robust, efficient, and broadband shg of ultrashort pulses in composite crystals. *Optics letters*, 44(15):3837–3840, 2019.
- [31] Elica Kyoseva, Hadar Greener, and Haim Suchowski. Detuning-modulated composite pulses for high-fidelity robust quantum control. *Physical Review A*, 100(3):032333, 2019.
- [32] Boyan T. Torosov and Nikolay V. Vitanov. High-fidelity composite quantum gates for raman qubits. *Phys. Rev. Research*, 2:043194, Nov 2020.
- [33] G. Dridi, M. Mejatty, S. J. Glaser, and D. Sugny. Robust control of a not gate by composite pulses. *Phys. Rev. A*, 101:012321, Jan 2020.
- [34] D. Zeuch and N. E. Bonesteel. Efficient two-qubit pulse sequences beyond cnot. *Phys. Rev. B*, 102:075311, Aug 2020.
- [35] Hayk L. Gevorgyan and Nikolay V. Vitanov. Ultrahigh-fidelity composite rotational quantum gates. *Phys. Rev. A*, 104:012609, Jul 2021.
- [36] Zhi-Cheng Shi, Hai-Ning Wu, Li-Tuo Shen, Jie Song, Yan Xia, X. X. Yi, and Shi-Biao Zheng. Robust single-qubit gates by composite pulses in three-level systems. *Phys. Rev. A*, 103:052612, May 2021.
- [37] Boyan T. Torosov and Nikolay V. Vitanov. Narrowband composite two-qubit phase gates. 6 2022.
- [38] Boyan T. Torosov and Nikolay V. Vitanov. Fast high-fidelity composite gates in superconducting qubits: Beating the Fourier leakage limit. 5 2022.
- [39] Moshe Katzman, Yonatan Piasezky, Evyatar Rubin, Ben Barenboim, Maayan Priel, Muhammad Erew, Avi Zadok, and Haim Suchowski. Robust directional couplers for state manipulation in silicon photonic-integrated circuits. *Journal of Lightwave Technology*, pages 1–1, 2022.
- [40] A. J. Shaka. Composite pulses for ultra-broadband spin inversion. *Chemical Physics Letters*, 120(2):201–205, 1985.

- [41] Kaveh Khodjasteh, Daniel Lidar, and Lorenza Viola. Arbitrarily accurate dynamical control in open quantum systems. *Physical review letters*, 104:090501, 03 2010.
- [42] Kaveh Khodjasteh and Lorenza Viola. Dynamical quantum error correction of unitary operations with bounded controls. *Physical Review A*, 80, 06 2009.
- [43] Navin Khaneja, Timo Reiss, Cindie Kehlet, T. Schulte-Herbrueggen, and Steffen Glaser. Optimal control of coupled spin dynamics: Design of nmr pulse sequences by gradient ascent algorithms. *Journal of magnetic resonance (San Diego, Calif. : 1997)*, 172:296–305, 03 2005.
- [44] Sakthi Thangavel, Radoslav Paulen, and Sebastian Engell. Robust multi-stage nonlinear model predictive control using sigma points. *Processes*, 8:851, 07 2020.
- [45] Thomas Propson, Brian Jackson, Jens Koch, Zac Manchester, and David Schuster. Robust quantum optimal control with trajectory optimization. *Physical Review Applied*, 17, 01 2022.
- [46] Jonathan C. F. Matthews, Alberto Politi, André Stefanov, and Jeremy L. O’Brien. Manipulation of multiphoton entanglement in waveguide quantum circuits. *Nature Photonics*, 3(6):346–350, 2009.
- [47] OIDA. Oida quantum photonics roadmap: Every photon counts. *OIDA*, page 3, Mar 2020.
- [48] Emanuele Pelucchi, Giorgos Fagas, Igor Aharonovich, Dirk Englund, Eden Figueroa, Qihuang Gong, Hübel Hannes, Jin Liu, Chao-Yang Lu, Nobuyuki Matsuda, Jian-Wei Pan, Florian Schreck, Fabio Sciarrino, Christine Silberhorn, Jianwei Wang, and Klaus D. Jöns. The potential and global outlook of integrated photonics for quantum technologies. *Nature Reviews Physics*, 4(3):194–208, Mar 2022.
- [49] Galan Moody, Volker J Sorger, Daniel J Blumenthal, Paul W Juodawlkis, William Loh, Cheryl Sorace-Agaskar, Alex E Jones, Krishna C Balram, Jonathan C F Matthews, Anthony Laing, Marcelo Davanco, Lin Chang, John E Bowers, Niels Quack, Christophe Galland, Igor Aharonovich, Martin A Wolff, Carsten Schuck, Neil Sinclair, Marko Lončar, Tin Komljenovic, David Weld, Shayan Mookherjea, Sonia Buckley, Marina Radulaski, Stephan Reitzenstein, Benjamin Pingault, Bartholomeus Machielse, Debsuvra Mukhopadhyay, Alexey Akimov, Aleksei Zheltikov, Girish S Agarwal, Kartik Srinivasan, Juanjuan Lu, Hong X Tang, Wentao Jiang, Timothy P McKenna, Amir H Safavi-Naeini, Stephan Steinhauer, Ali W Elshaari, Val Zwiller, Paul S Davids, Nicholas Martinez, Michael Gehl, John Chiaverini, Karan K Mehta, Jacqueline Romero, Navin B Lingaraju, Andrew M Weiner, Daniel Peace, Robert Cernansky, Mirko Lobino, Eleni Diamanti, Luis Trigo Vidarte, and Ryan M Camacho. 2022 roadmap on integrated quantum photonics. *Journal of Physics: Photonics*, 4(1):012501, jan 2022.
- [50] R.W. Boyd. *Nonlinear Optics*. Elsevier Science, 2020.
- [51] Diederik P. Kingma and Jimmy Ba. Adam: A method for stochastic optimization, 2017.
- [52] Meisam Bahadori, Mahdi Nikdast, Qixiang Cheng, and Keren Bergman. Universal design of waveguide bends in silicon-on-insulator photonics platform. *Journal of Light-wave Technology*, 37(13):3044–3054, 2019.
- [53] Ali Emre Kaplan, Gaetano Bellanca, Jorn P. van Engelen, Yuqing Jiao, Jos J. G. M. van der Tol, and Paolo Bassi. Experimental characterization of directional couplers in inp photonic membranes on silicon (imos). *OSA Continuum*, 2(10):2844–2854, Oct 2019.
- [54] John Preskill. Quantum computing in the nisq era and beyond. *Quantum*, 2, 7 2018.
- [55] Austin G. Fowler, Matteo Mariantoni, John M. Martinis, and Andrew N. Cleland. Surface codes: Towards practical large-scale quantum computation. *Phys. Rev. A*, Oct 2012.
- [56] Robert Raussendorf, Dan E. Browne, and Hans J. Briegel. Measurement-based quantum computation on cluster states. *Physical Review A*, 68(2):022312–022312, 2003.
- [57] Navin Khaneja, Timo Reiss, Cindie Kehlet, Thomas Schulte-Herbrüggen, and Steffen J. Glaser. Optimal control of coupled spin dynamics: design of nmr pulse sequences by gradient ascent algorithms. *Journal of Magnetic Resonance*, 172(2):296–305, 2005.
- [58] Yuquan Chen, Yajie Hao, Ze Wu, Bi-Ying Wang, Ran Liu, Yanjun Hou, Jiangyu Cui, Man-Hong Yung, and Xinhua Peng. Iterative gradient ascent pulse engineering algorithm for quantum optimal control, 2022.
- [59] Thomas Propson, Brian E. Jackson, Jens Koch, Zachary Manchester, and David I. Schuster. Robust quantum optimal control with trajectory optimization. 2021.
- [60] Amnon Yariv. *Quantum Electronics*. Wiley, New York, 3rd ed. edition, 1989.

Appendix A: Perturbative Solutions for Fully Correlated Detuning Errors

1. iX gate in 3 segments

A first-order solution for the iX gate in 3 segments is given by:

$$\Omega_1 = \Omega, \quad \Delta_1 = \Delta, \quad t_1 = \frac{\pi}{\sqrt{\Omega^2 + \Delta^2}}, \quad (\text{A1a})$$

$$\Omega_2 = \frac{\Omega^2 + \Delta^2}{2\Omega}, \quad \Delta_2 = 0, \quad t_2 = \frac{2\pi\Omega}{\Omega^2 + \Delta^2}, \quad (\text{A1b})$$

$$\Omega_3 = \Omega, \quad \Delta_3 = -\Delta, \quad t_3 = \frac{\pi}{\sqrt{\Omega^2 + \Delta^2}}, \quad (\text{A1c})$$

where $\Omega > 0$ and Δ are free parameters. Examples of this solution are fully presented in Table I, and their fidelities are shown in Fig. 8(a). One can see clearly how the fidelity improves with the composite design.

Composite iX gate in 3 segments			
solution	Ω_1, Δ_1, t_1	Ω_2, Δ_2, t_2	Ω_3, Δ_3, t_3
$\Delta_1 = 0.5\Omega$	1.00, 0.500, 2.81	0.625, 0, 5.03	1.00, -0.500, 2.81
$\Delta_1 = 0.75\Omega$	1.00, 0.750, 2.51	0.781, 0, 4.02	1.00, -0.750, 2.51
$\Delta_1 = 1\Omega$	1.00, 1.00, 2.22	1.00, 0, 3.14	1.00, -1.00, 2.22
$\Delta_1 = 1.1\Omega$	1.00, 1.1, 2.11326	1.105, 0, 2.84307	1.00, -1.1, 2.11326
$\Delta_1 = 1.2\Omega$	1.00, 1.2, 2.0112	1.22, 0, 2.57508	1.00, -1.2, 2.0112

TABLE I. Examples of iX gate generated by Eq. (A1), such that the couplings and detunings are of the same order. The fidelity of these gates compared to the one-segments iX gate are shown in Fig. 8(a).

2. $(iX)^{\frac{1}{n}}$ gate in 3 segments

A first-order solution for the $(iX)^{\frac{1}{n}}$ gate in 3 segments is given by:

$$\Omega_1 = \Omega, \quad \Delta_1 = 0, \quad t_1 = \frac{\theta}{\Omega}, \quad (\text{A2a})$$

$$\Omega_2 = \frac{\sin\left(\theta + \frac{\pi}{2n}\right)}{\sin\left(\theta + \frac{\pi}{2n}\right) - \sin\left(\frac{\pi}{2n}\right)}\Omega, \quad \Delta_2 = 0, \quad (\text{A2b})$$

$$t_2 = \frac{2\left(2\pi m - \theta - \frac{\pi}{2n}\right)}{\Omega_2},$$

$$\Omega_3 = \Omega, \quad \Delta_3 = 0, \quad t_3 = \frac{\theta}{\Omega}, \quad (\text{A2c})$$

where $\Omega > 0$ and θ are free real parameters and m is a free integer parameter (with the constraint $t_2 > 0$). Examples of this solution for $n = 2, 3$ are presented in Tables II, III, and their fidelities are shown in Figs. 8(b)+(c), where $m = 1$ where chosen for all of them. One can see clearly how the fidelity improves with the composite design.

3. Other families of solutions for $(iX)^{\frac{1}{n}}$

We found additional first-order solutions for $(iX)^{\frac{1}{n}}$:

1.
$$\Omega_1 = \Omega, \quad \Delta_1 = 0, \quad t_1 = \frac{\pi}{\Omega}, \quad (\text{A3a})$$

Composite $(iX)^{\frac{1}{2}}$ gate in 3 segments			
solution	Ω_1, Δ_1, t_1	Ω_2, Δ_2, t_2	Ω_3, Δ_3, t_3
$\theta = \frac{\pi}{2.2}$	1.00, 0, 1.428	8.56794, 0, 0.950004	1.00, 0, 1.428
$\theta = \frac{\pi}{2.4}$	1.00, 0, 1.309	5.44949, 0, 1.53731	1.00, 0, 1.309
$\theta = \frac{\pi}{2.6}$	1.00, 0, 1.2083	4.45279, 0, 1.92665	1.00, 0, 1.2083
$\theta = \frac{\pi}{2.8}$	1.00, 0, 1.122	3.98639, 0, 2.19537	1.00, 0, 1.122
$\theta = \frac{\pi}{3}$	1.00, 0, 1.05	3.73, 0, 2.39	1.00, 0, 1.05
$\theta = \frac{\pi}{4}$	1.00, 0, 0.785	3.41, 0, 2.76	1.00, 0, 0.785
$\theta = \frac{\pi}{5}$	1.00, 0, 0.628	3.52, 0, 2.77	1.00, 0, 0.628

TABLE II. Examples of $(iX)^{\frac{1}{2}}$ gate generated by Eq. (A2) (with $n = 2$ and choosing $m = 1$), such that the couplings and detunings are of the same order. The fidelity of these gates compared to the one-segments $(iX)^{\frac{1}{2}}$ gate are shown in Fig. 8(b).

Composite $(iX)^{\frac{1}{3}}$ gate in 3 segments			
solution	Ω_1, Δ_1, t_1	Ω_2, Δ_2, t_2	Ω_3, Δ_3, t_3
$\theta = \frac{\pi}{1.8}$	1.00, 0, 1.74533	2.87939, 0, 2.78827	1.00, 0, 1.74533
$\theta = \frac{\pi}{2.2}$	1.00, 0, 1.428	2.16722, 0, 3.99737	1.00, 0, 1.428
$\theta = \frac{\pi}{2.4}$	1.00, 0, 1.309	2.07313, 0, 4.29359	1.00, 0, 1.309
$\theta = \frac{\pi}{2.6}$	1.00, 0, 1.2083	2.02659, 0, 4.49157	1.00, 0, 1.2083
$\theta = \frac{\pi}{2.8}$	1.00, 0, 1.122	2.00562, 0, 4.62459	1.00, 0, 1.122
$\theta = \frac{\pi}{3}$	1.00, 0, 1.05	2.00, 0, 4.71	1.00, 0, 1.05
$\theta = \frac{\pi}{4}$	1.00, 0, 0.785	2.07, 0, 4.80	1.00, 0, 0.785
$\theta = \frac{\pi}{5}$	1.00, 0, 0.628	2.21, 0, 4.65	1.00, 0, 0.628
$\theta = \frac{\pi}{6}$	1.00, 0, 0.524	2.37, 0, 4.43	1.00, 0, 0.524
$\theta = \frac{\pi}{7}$	1.00, 0, 0.449	2.53, 0, 4.19	1.00, 0, 0.449

TABLE III. Examples of $(iX)^{\frac{1}{3}}$ gate generated by Eq. (A2) (with $n = 3$ and choosing $m = 1$) such that the couplings and detunings are of the same order. The fidelity of these gates compared to the one-segments $(iX)^{\frac{1}{3}}$ gate are shown in Fig. 8(c).

$$\Omega_2 = \frac{\Omega}{2}, \quad \Delta_2 = 0, \quad t_2 = \frac{2\left(2\pi - \frac{\pi}{n}\right)}{\Omega}, \quad (\text{A3b})$$

$$\Omega_3 = \Omega, \quad \Delta_3 = 0, \quad t_3 = \frac{\pi}{\Omega}, \quad (\text{A3c})$$

where $\Omega > 0$ is a free real parameter.

2.

$$\Omega_1 = \Omega, \quad \Delta_1 = \Delta, \quad t_1 = \frac{2\pi}{\sqrt{\Omega^2 + \Delta^2}}, \quad (\text{A4a})$$

$$\Omega_2 = \frac{(\sqrt{\Omega^2 + \Delta^2})^{\frac{3}{2}}}{2\pi\Delta^2} \tan\left(\frac{\pi}{2n}\right), \quad \Delta_2 = 0, \quad (\text{A4b})$$

$$t_2 = \frac{2\left(2\pi - \frac{\pi}{2n}\right)}{\Omega_2},$$

$$\Omega_3 = \Omega, \quad \Delta_3 = -\Delta, \quad t_3 = \frac{2\pi}{\sqrt{\Omega^2 + \Delta^2}}, \quad (\text{A4c})$$

where $\Omega > 0$ and Δ are free real parameters.

3.

$$\Omega_1 = \Omega, \quad \Delta_1 = \Delta, \quad (\text{A5a})$$

$$t_1 = \frac{2\left(m\pi - \arctan\left(\sqrt{1 + \frac{\Delta^2}{\Omega^2}} \tan\left(\frac{\pi}{2n}\right)\right)\right)}{\sqrt{\Omega^2 + \Delta^2}},$$

Composite iX gate in 4 segments with same coupling for each				
solution	Ω_1, Δ_1, t_1	Ω_2, Δ_2, t_2	Ω_3, Δ_3, t_3	Ω_4, Δ_4, t_4
$\xi \approx 0.46097$	1.00, 0, 4.71	1.00, 0.460966, 5.70612	1.00, -0.460966, 5.70612	1.00, 0, 4.71
$\xi \approx 6.03285$	1.00, 0, 4.71	1.00, 6.03285, 1.02748	1.00, -6.03285, 1.02748	1.00, 0, 4.71

TABLE IV. The two 4-segments composite iX gates given by Eq. (A6). The fidelity of these gates compared to the one-segments iX gate are shown in Fig. 8(d).

$$\Omega_2 = \frac{(\Omega^2 + \Delta^2) \sin\left(\frac{\pi}{2n}\right)}{2\Omega \sin\left(\frac{\pi}{2n}\right) - t_1 \Delta^2 \cos\left(\frac{\pi}{2n}\right)}, \quad \Delta_2 = 0, \quad t_2 = \frac{\pi}{n\Omega_2}, \quad (\text{A5b})$$

$$\begin{aligned} \Omega_3 &= \Omega, \quad \Delta_3 = -\Delta, \\ t_3 &= \frac{2\left(m\pi - \arctan\left(\sqrt{1 + \frac{\Delta^2}{\Omega^2}} \tan\left(\frac{\pi}{2n}\right)\right)\right)}{\sqrt{\Omega^2 + \Delta^2}}, \end{aligned} \quad (\text{A5c})$$

where $\Omega > 0$ and Δ are free real parameters, and m is a free integer parameter (with the constraint $t_1 > 0$).

4. iX gate in 4 segments with constant coupling

A first-order solution for the iX gate in 4 segments with equal couplings:

$$\Omega_1 = \Omega, \quad \Delta_1 = 0, \quad t_1 = \frac{4 \arctan(1 + \sqrt{2})}{\Omega}, \quad (\text{A6a})$$

$$\Omega_2 = \Omega, \quad \Delta_2 = \xi\Omega, \quad t_2 = \frac{2\pi}{\sqrt{\Omega^2 + \Delta_2^2}}, \quad (\text{A6b})$$

$$\Omega_3 = \Omega, \quad \Delta_3 = -\xi\Omega, \quad t_3 = \frac{2\pi}{\sqrt{\Omega^2 + \Delta_2^2}}, \quad (\text{A6c})$$

$$\Omega_4 = \Omega, \quad \Delta_4 = 0, \quad t_4 = \frac{4 \arctan(1 + \sqrt{2})}{\Omega}, \quad (\text{A6d})$$

where Ω is a free real parameter and ξ is one of the two positive solutions of the equation $(2\pi\xi^2)^2 = (1 + \xi^2)^3$ (i.e., $\xi \approx 0.461, 6.033$). These two solutions are summarized in Table IV, and their fidelities are shown in Fig. 8(d). One can see clearly how the fidelity improves with the composite design.

5. The fidelity of the composite gates

In Fig. 8, we present the results of the composite gates. We show the fidelity of our composite gates compared to regular uniform ones. The parameters of the segments were given in previous subsections of this section. Note that in these plots we consider the fidelity as a deterministic object and plot its values as a function of the values of the error.

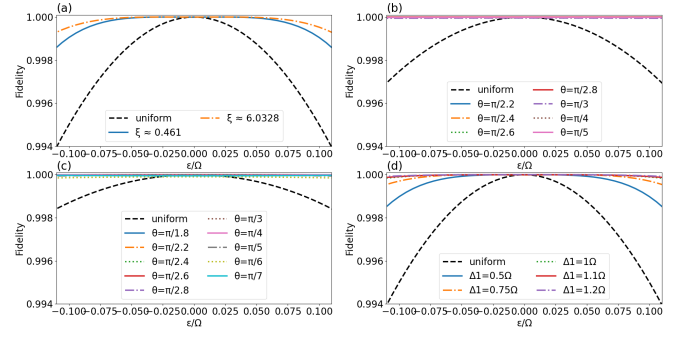


FIG. 8. (a) The fidelity of examples of the composite iX gate in 3 segments given by Eq. (A1), compared to the one-segments case as a function of the detuning error. These parameters are given in Table I. (b) The fidelity of examples of the composite $(iX)^{\frac{1}{2}}$ gate in 3 segments given by Eq. (A2), compared to the one-segments case. The parameters are given in Table II. (c) The fidelity of examples of the composite $(iX)^{\frac{1}{3}}$ gate in 3 segments given by Eq. (A2), compared to the one-segments case. The parameters are given in Table III. (d) The fidelity of the two 4-segment composite iX gates given by Eq. (A6), compared to the one-segments case. The parameters are given in Table IV. We see the robustness of the segmented design in comparison to the uniform one.

Composite gates in 3 segments			
Gate	Ω_1, Δ_1, t_1	Ω_2, Δ_2, t_2	Ω_3, Δ_3, t_3
X	1.06, 1.784, 1.521	2.029, -0.005, 1.547	1.048, -1.776, 1.516
$X^{\frac{1}{2}}$	2.043, 0.2884, 2.0	5.763, -1.8525, 2.0	2.043, 0.2885, 2.0
$X^{\frac{1}{3}}$	3.629, 0.2737, 7.0	3.607, -0.4956, 7.0	3.6319, 0.259, 7.0
H	4.773, -0.978, 2.0	1.1855, 0.5415, 2.0	1.7075, -0.31135, 2.0

TABLE V. Examples of non-perturbative solutions using the fully correlated detuning error model.

Appendix B: Non-Perturbative Solutions for Fully Correlated Detuning Errors

Using the parameters optimization algorithm described in Section C, we generated optimization solutions for the following gates: X , $X^{\frac{1}{2}}$, $X^{\frac{1}{3}}$, H , resulting in the parameters given in Table V. Note that each of the gates constructed using these parameters is multiplied by a global phase. The fidelity of the resulting gates is compared to the one-segments gates in Fig. 9.

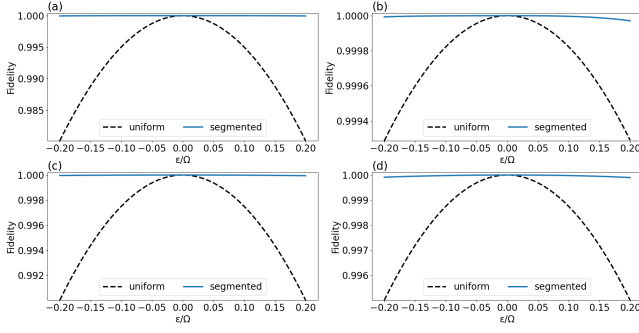


FIG. 9. The fidelity of examples of the composite gates in 3 segments generated by the optimization algorithm compared to the one-segments case, as a function of the detuning error. In (a) the ideal gate is X , in (b) the ideal gate is the Hadamard gate, in (c) the ideal gate is $X^{\frac{1}{2}}$ and in (d) the ideal gate is $X^{\frac{1}{3}}$. All gates are calculated up to the global phase. These examples are given in Table V. We see the robustness of the segmented design in comparison to the uniform one.

Appendix C: Detailed explanation regarding the numeric approach methodology

In this section, we will describe in further details the optimization process of the numeric, non-perturbative method, and we will exemplify the process using the detuning error model. As stated before, the non-perturbative approach generates optimized parameters by using a loss function which is composed of two subfunctions:

1. Value range loss subfunction — returns the sum:

$$\begin{aligned} & \sum_{i=0}^{N-1} \max(0, -t_i) + \max(0, \Omega_{\max} - \Omega_i) + \\ & \max(0, \Omega_i - \Omega_{\min}) + \max(0, \Delta_{\max} - \Delta_i) + \\ & \max(0, \Delta_i - \Delta_{\min}). \end{aligned} \quad (\text{C1})$$

This subfunction ensures that the parameters we obtain are within their legal value range (t_i values measure the length of the waveguides, which means they cannot be negative; the detuning and coupling parameters have a range of feasible values they can be in).

2. Robust fidelity loss — returns the fidelity between the error-less matrix and a range of matrices created by using current parameters $\Omega_i, \Delta_i, t_i, i \in \{0, 1, \dots, N-1\}$.

This robust fidelity loss is calculated in the following way:

1. Set vector X to be a vector of n numbers evenly spaced between -3σ to 3σ ; $X = [-3\sigma, -3\sigma + \frac{6\sigma}{n-1}, -3\sigma + 2\frac{6\sigma}{n-1}, \dots, 3\sigma - \frac{6\sigma}{n-1}, 3\sigma]$, where n is the number of error values used for the optimization (varies between optimization processes, in the range of 2,500 to 10,000).
2. Set vector Dist to be the given error distribution vector; for example, a Gaussian distributed vector is calculated as $\text{Dist} = [a_{-n/2+1}, a_{-n/2+2}, \dots, a_0, \dots, a_{n/2-2}, a_{n/2-1}]$, where $a_i = \frac{1}{\sigma \cdot \sqrt{2\pi}} \cdot e^{-\frac{x_i^2}{2\sigma^2}}$.
3. Use the current parameters $\Omega_i, \Delta_i, t_i, i \in \{0, 1, \dots, N-1\}$ and create n waveguide matrices, differing in the

value of the error $\delta\Delta$; $\delta\Delta$ of the matrix M_i is the element x_i of the vector X :

$$M_i = U_3(\Omega_0, \Delta_0 + x_i, t_0, \Omega_1, \Delta_1 + x_i, t_1, \Omega_2, \Delta_2 + x_i, t_2).$$

4. Calculate the fidelity loss of all these matrices and store them in vector F :

$$F_i = F_{\text{loss}}(U_{\text{ideal}}, M_i),$$

where $F_{\text{loss}}(U_{\text{ideal}}, U) = 1 - F_{\text{norm}}(U_{\text{ideal}}, U)$ and $F_{\text{norm}}(U_{\text{ideal}}, U) = |\text{Tr}(U_{\text{ideal}}^\dagger U)|/2$

5. Return $F \cdot \text{Dist}$ (scalar product between the vectors).

Minimizing these subfunctions increases the overall fidelity robustness while keeping the parameters in their previously approved range. Generally, the optimizer used was the Adam optimizer with a learning rate of 10^{-3} , but some gates were more delicate (for instance, $X^{0.5}$) and required a smaller learning rate. The optimization also worked well with a stochastic gradient descent optimizer.

Appendix D: The parameters of directional couplers as a function of distance and widths

In order to estimate the detuning and coupling coefficients corresponding to the geometric parameters, we used Lumerical, a commercially available finite difference eigenmode solver. We solved for the fields and effective mode indices $E(w), H(w), n(w)$ for different widths w . With these solutions, we were able to approximate the dynamics parameters, using the coupled-mode theory perturbative approximation [60]:

$$m_i \triangleq \frac{\omega}{4} \iint [\epsilon(x, y) - \epsilon^{(i)}(x, y)] (\vec{E}_\perp(w_i))^2 dx dy, \quad (\text{D1a})$$

$$\Delta = \Delta\beta(w_1, w_2, g) \approx \frac{2\pi}{\lambda} (n_1 - n_2) + M_1 - M_2, \quad (\text{D1b})$$

$$\begin{aligned} \Omega &= \kappa(w_1, w_2, g) \approx \\ & \frac{\omega}{4} \iint [\epsilon(x, y) - \epsilon^{(2)}(x, y)] \vec{E}_\perp(w_1) \cdot \vec{E}_\perp(w_2) dx dy, \end{aligned} \quad (\text{D1c})$$

where $\epsilon^{(i)}$ is defined as the permittivity distribution in space when only waveguide i exists. m_1 and m_2 represent small corrections to the propagation constants, β_1 and β_2 , respectively, because of the presence of the second waveguide.

To be able to use this in the perturbative method or in gradient-based optimization algorithms, we performed this evaluation for a large number of geometries within our range of interest, and a multidimensional interpolation function was derived. The use of the coupled mode theory approximation enabled us to do so with a number of simulations that grows linearly with the number of different widths, and as a constant with respect to the number of gaps, instead of a number that grows as the number of widths squared times the number of gaps, as was needed for a more precise supermodes solution. The widths we took are between 300 and 400 nm, and the gaps we took are between 800 and 1200 nm.

By calculating Eq. (D1) for different width values for the two waveguides, we obtain a grid of width values, which are correlated to a grid of detuning and coupling coefficients, as can be seen in figure 10. After obtaining this grid, we used

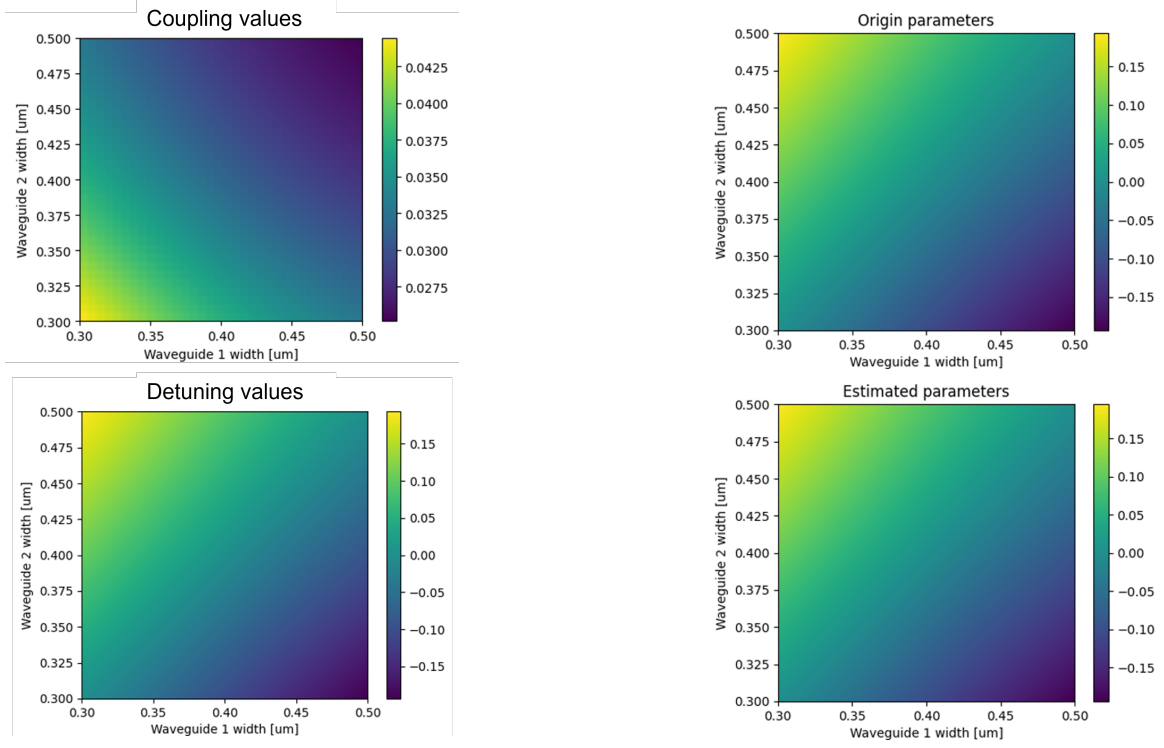


FIG. 10. Grid of waveguide widths mapped to coupling and detuning coefficient values

fitting algorithms in order to fit polynomial and exponential functions to the data.

For the detuning coefficient, a Taylor series in the form below was used (where w_i is the width of waveguide i):

$$\Delta = \sum_{i=0}^4 a_i \cdot w_1^i + b_i \cdot w_2^i$$

In figure 11, we can see how the approximate function behaves similarly to the values generated from the Lumerical simulations, where the average difference between the matrices is 0.00022, which translated to $\sim 1\%$ of the detuning coefficient.

For the Coupling coefficient, the following exponential function was used:

$$\Omega = a_0 + a_1 \cdot (w_1 + w_2) \cdot e^{a_2 \cdot (w_1 + w_2)}$$

In figure 12, we can see how the estimating function behaves similarly to the values generated from the CMT approximation, where the average difference between the matrices is 0.00017, which translated to $\sim 0.5\%$ of the coupling coefficient.

Lastly, we corrected the inaccuracies resulting from the coupled mode theory approximation as follows: We used the interpolation function to find the optimal composite design. We then calculated the expected rotation angle for each segment, $\theta = \Omega_g L$, where $\Omega_g = \sqrt{\Omega^2 + \Delta^2}$ is the generalized coupling coefficient. Then, in Lumerical, we solved for the generalized coupling coefficient of the selected segment using the more precise supermodes method [60]. In this method, we solved for the modes of both waveguides together, unlike the coupled mode theory, where we solve for each mode separately and assume that the coupling is weak. The length of the segment

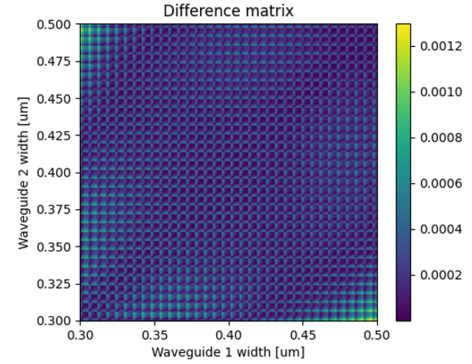


FIG. 11. Comparison between the fit function estimation and the original detuning grid.

is then determined from the desired rotation angle and the precise generalized coupling coefficient.

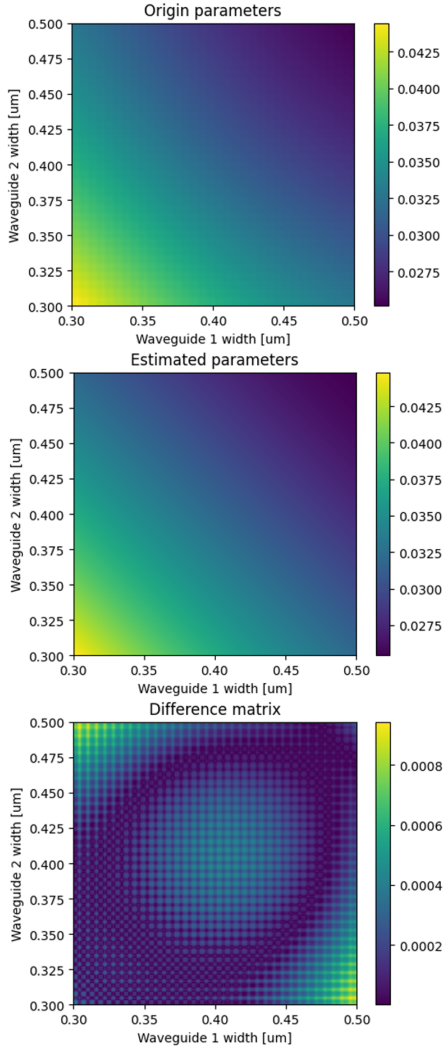


FIG. 12. Comparison between the fit function estimation and the original coupling grid.

Appendix E: The geometrical parameters of the robust segmented gates

Here we present selected solutions achieved from both approaches described in Sec. III B. The parameters generated by the perturbative approach is presented in table VI, and parameters generated by the non-perturbative approach is presented in table VII. The gap between the two waveguides for all these solutions is $1.2\mu\text{m}$.

Composite gates in 3 segments based on the model of correlated errors of widths				
the gate	$w_{a_{uni}}, w_{b_{uni}}, z_{uni}$ [μm]	w_{a_1}, w_{b_1}, z_1 [μm]	w_{a_2}, w_{b_2}, z_2 [μm]	w_{a_3}, w_{b_3}, z_3 [μm]
$-iX$	0.450, 0.45, 79.44	0.4857, 0.4345, 47.1117	0.4057, 0.4896, 40.5109	0.4857, 0.4345, 47.1117
$(iX)^{\frac{1}{2}}$	0.4, 0.4, 118.972	0.426, 0.387, 79.892	0.318, 0.499, 55.8067	0.426, 0.387, 79.892
iH	0.426, 0.460, 58.8037	0.379, 0.486, 29.6481	0.5, 0.31, 53.75	0.379, 0.486, 29.6481
$\sqrt{\frac{1}{3}}I - i\sqrt{\frac{2}{3}}X$	0.450, 0.45, 35.278	0.358, 0.457, 21.890	0.485, 0.34, 28.0211	0.358, 0.457, 21.890

TABLE VI. Selected robust segmented gates achieved by the perturbative approach. These gates are robust against correlated errors in the widths.

Composite gates in 3 segments based on the model of correlated errors of widths				
the gate	$w_{a_{uni}}, w_{b_{uni}}, z_{uni}$ [μm]	w_{a_1}, w_{b_1}, z_1 [μm]	w_{a_2}, w_{b_2}, z_2 [μm]	w_{a_3}, w_{b_3}, z_3 [μm]
$-iX$	0.450, 0.45, 79.44	0.375, 0.425, 49.254	0.429, 0.363, 52.608	0.391, 0.45, 46.63
$(iX)^{\frac{1}{2}}$	0.4, 0.4, 20.0872	0.48, 0.326, 15.28	0.32, 0.478, 28.402	0.48, 0.324, 15.18
iH	0.426, 0.460, 58.8037	0.430, 0.452, 70.29	0.422, 0.325, 33.522	0.430, 0.452, 70.328
$\sqrt{\frac{1}{3}}I - i\sqrt{\frac{2}{3}}X$	0.450, 0.45, 35.278	0.351, 0.46, 20.468	0.459, 0.34, 34.078	0.349, 0.46, 20.261

TABLE VII. Selected robust segmented gates achieved by the non-perturbative approach. These gates are robust against correlated errors in the widths.

Appendix F: The fidelity of composite gates using different error distributions

In order to ensure that the results presented in the article aren't only relevant to Gaussian error distribution, we added simulations of the fidelity using various additional error distributions, as can be seen in the Fig 13.

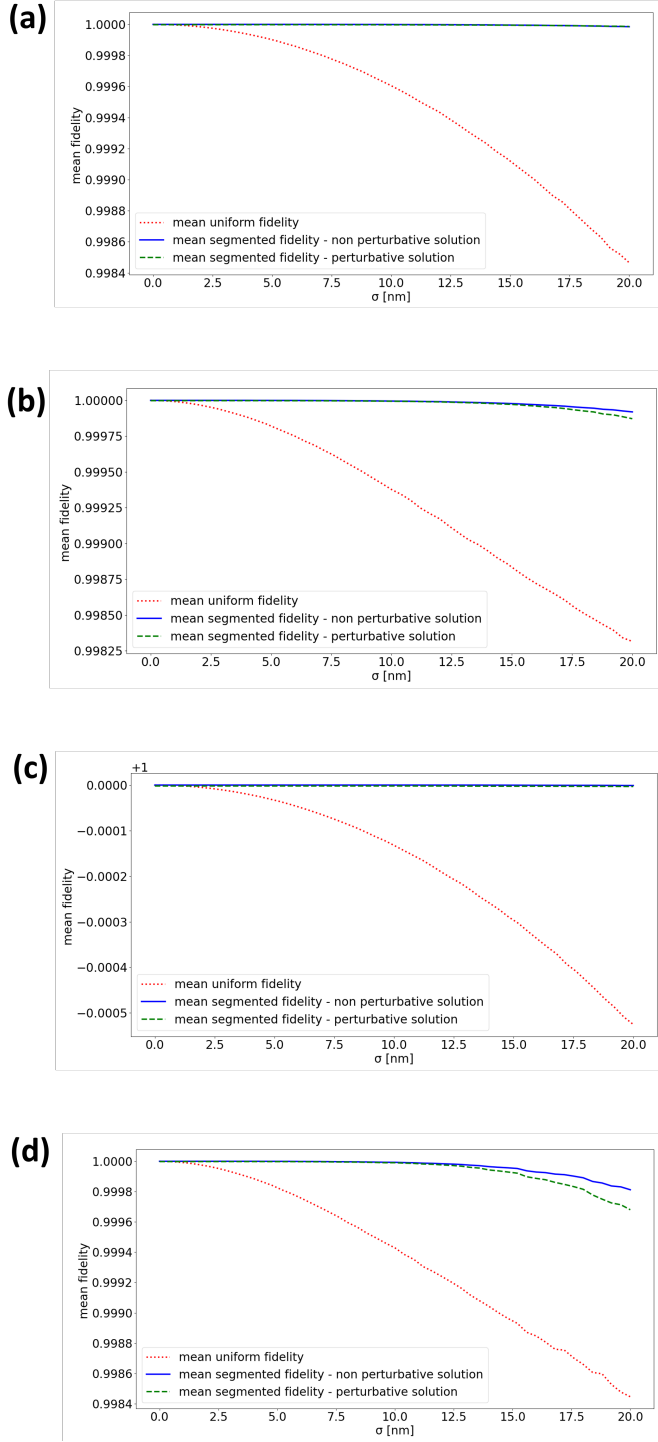


FIG. 13. The mean fidelity of the perturbative and non-perturbative composite gates compared to uniform gates, with full error correlation in the width, as a function of the error standard deviation σ , using different error distributions, where the ideal gate is X . In (a) the error distribution is Gaussian, in (b) the error distribution is Poisson (where $\lambda = 1$ and the result is multiplied by the value of σ), in (c) the error distribution is Uniform (uniform distribution between -3σ and 3σ) and in (d) the error distribution is exponential.